

Elucidating the formation and structural evolution of platinum single-site catalysts for hydrogen evolution reaction

Peng Tang¹, Hyeon Jeong Lee¹, Kevin Hurlbutt¹, Po-Yuan Huang¹, Sudarshan Narayanan¹, Chenbo Wang², Diego Gianolio⁵, Rosa Arrigo⁶, Jun Chen¹, Jamie H. Warner^{3,4}, and Mauro Pasta^{1,2}

¹Department of Materials, University of Oxford, Parks Road, Oxford OX1 3PH, United Kingdom

²Oxford Suzhou Centre for Advanced Research, 388 Ruoshui Road, Suzhou 215123, Jiangsu Province, P. R. China

³Materials Graduate Program, Texas Materials Institute, The University of Texas at Austin, 204 East Dean Keeton Street, Austin, Texas, 78712, United States

⁴Walker Department of Mechanical Engineering, The University of Texas at Austin, 204 East Dean Keeton Street, Austin, Texas, 78712, United States

⁵Diamond Light Source Ltd., Harwell Science and Innovation Campus, Chilton, Didcot, OX11 0DE, UK

⁶ School of Science, Engineering and Environment, University of Salford, M5 4WT Manchester, U.K

Abstract

Platinum single-site catalysts (SSCs) are a promising technology for the production of hydrogen from clean energy sources. They have high activity and maximal platinum-atom utilisation. However, the bonding environment of platinum during operation is poorly understood. In this work, we use operando, synchrotron-X-ray absorption spectroscopy to study the platinum bonding in SSCs. First, we synthesise an atomically dispersed platinum complex with aniline and chloride ligands onto graphene and characterise it with ex-situ electron microscopy, X-ray diffractometry, X-ray photoelectron spectroscopy, X-ray absorption near edge structure spectroscopy (XANES), and extended X-ray absorption fine structure spectroscopy (EXAFS). Then, by operando EXAFS and XANES, we show that as a negatively biased potential is applied, the Pt-N bonds break first followed by the Pt-Cl bonds. The platinum is reduced from platinum(II) to metallic platinum(0) by the onset of the hydrogen-evolution reaction at 0 V. Furthermore, we observe an increase in Pt-Pt bonding, indicating the formation of platinum agglomerates. Together, these results indicate that while aniline is used to prepare platinum SSCs, the single-site complexes are decomposed and platinum agglomerates at operating potentials. This work is an important contribution to the understanding of the bonding environment and the evolution of the molecular structure of platinum complexes in SSCs.

Introduction

Catalysts for the electrochemical hydrogen evolution reaction (HER) are desirable to be able to produce

hydrogen from clean sources like solar energy. [1, 2] Platinum is among the most active HER catalysts known in acidic media. [3] Platinum is a heterogeneous catalyst, with the HER occurring only

on the metal surface.[4] This can be prohibitively inefficient because platinum is so rare and expensive. [5]

Single-atom catalysts (SACs) are systems in which electrocatalytically active metal atoms are loaded onto a suitable substrate and separated from any other metal atoms by a distance larger than their metallic bonding. [6, 7] They have extremely high atom utilisation because every catalytic atom is exposed to the reactants and available for reaction. [8, 9]

Platinum SACs can be prepared by synthesising a platinum complex and adsorbing the whole complex to a suitable substrate. [10–12] We choose to distinguish these structures and refer to them as single-site catalysts (SSCs). This is to emphasise that these structures have well-separated sites of catalysis, but, as complexes, they are composed of multiple atoms. [13–15]

Despite the promise of platinum SSCs for the HER, the bonding environment of platinum in these devices before and during operation is poorly understood. [16–19] Establishing the structure-property relationship between the platinum bonding and the electrochemical performance of the catalyst is critically important to enabling design of tailored, high performing platinum SSCs. [20, 21]

In this work we examine the model SSC system of a platinum complex with aniline and chloride ligands adsorbed onto graphene. Graphene is an excellent substrate because of its high electronic conductivity, chemical stability, [22] and the good contrast it provides with platinum in electron microscopy. [23] At the same time, aniline is stabilised on adsorption onto graphene through pi-pi stacking interactions with the molecule’s aromatic ring. [10] Furthermore, aniline readily complexes with platinum and the molecule’s large size provides a steric hindrance that can prevent platinum agglomeration. [24, 25]

We characterise the morphology and physical structure of the as-synthesised SSC with ex-situ scanning transmission electron microscopy (STEM) and X-ray diffractometry (XRD). We examine the SSC’s oxidation state and bonding environment with photoelectron spectroscopy (XPS), X-ray absorption near edge structure spectroscopy (XANES), and extended X-ray absorption fine structure spectroscopy (EXAFS). Finally, we use chronoamperometry with operando, synchrotron EXAFS and XANES to study how the platinum’s bonding environment and coordination number

change as a function of applied potential during the HER. This work is an important contribution to the understanding of the synthesis and stability of platinum SSCs.

Results and Discussion

Synthesis and physiochemical characterisation

The platinum SSC is prepared according to a modified impregnation method described in detail in the Experimental procedures section and outlined in Figure 1a.

High-angle annular dark-field scanning transmission electron microscopy (HAADF-STEM) of (Pt/Ani/Ar) and (Pt/Ar) are shown in Figure 1c-d and e-f, respectively. (Pt/Ani/Ar) contains atomically dispersed platinum with an average areal number density of about 0.5 nm^{-2} (Supplementary Figure S2a). Some clusters of platinum are present; [25] these are generally of size 1 nm or smaller (Supplementary Figure S2a). (Pt/Ar) mainly contains larger nanoparticles that are up to about 4 nm across (Supplementary Figure S2b).

The XRD patterns for the glassy carbon (GC) electrode and for (Pt/Ani/Ar) are shown in Figure 1b. [26] The two patterns match well. In particular, the pattern for (Pt/Ani/Ar) lacks the intense peaks at about 39.8° , 46.2° , and 68.5° expected for the (111), (200), and (220) reflections in crystalline platinum (PDF#04-0802). This implies that the HAADF-STEM images, which show no platinum nanoparticles in (Pt/Ani/Ar), are representative of the bulk sample. The STEM images show that treatment with aniline promotes the formation of more atomically dispersed platinum.

Ex-situ XPS and XAS

The platinum oxidation state is investigated by XPS, and the spectra for (Pt/Ani/Ar) and (Pt/Ar) are shown in Figure 2a. Two standards are also shown: ammonium hexachloroplatinate(IV) $((\text{NH}_4)_2\text{PtCl}_6)$ and platinum(II) chloride (PtCl_2) . The platinum $4f_{7/2}$ peak in PtCl_2 has a binding energy of 72.9 eV consistent with the +2 oxidation state. The $(\text{NH}_4)_2\text{PtCl}_6$ has a higher binding energy of 75.2 eV, which is also expected for its high oxidation state of +4. The spectrum for (Pt/Ani/Ar) is well fitted by a 74% contribution from a peak centred

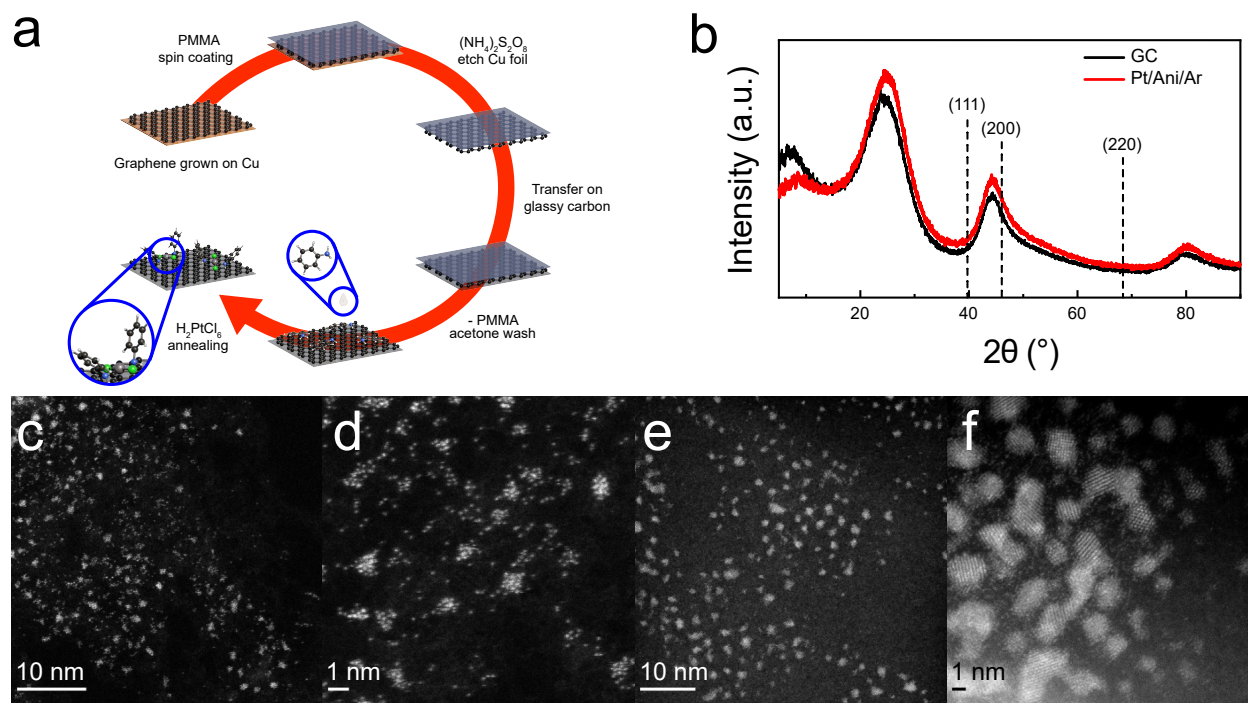


Figure 1. **a**, Schematic illustration of the synthesis process (5 steps) for Pt SSC (grey, Pt; green, Cl; blue, N; black, carbon; white, H). Step 1: graphene nanosheets are grown by chemical vapour deposition (CVD) on copper; Step 2: copper foil is etched after spin-coating with polymethyl methacrylate (PMMA) on top; Step 3: Thin-layer graphene coated with PMMA is then transferred onto a polished glassy carbon (GC) electrode; Step 4: after washing the PMMA with acetone and heating to 250 °C to remove trace organic contaminants, aniline is drop-cast onto the graphene-coated GC electrode and dried; Step 5: chloroplatinic acid in ethanol is then drop-cast and annealed under argon atmosphere. This sample is referred to as the (Pt/Ani/Ar) sample. The control sample (Pt/Ar) is prepared by the same method but without aniline. **b**, X-ray diffraction patterns for pristine GC and a (Pt/Ani/Ar) sample on GC; low magnification to high magnification atomic resolution HAADF-STEM images of (Pt/Ani/Ar) (**c**, **d**) and Pt/Ar (**e**, **f**).

at 72.8 ± 0.1 eV and a 26% contribution from a peak centred at 74.6 ± 0.1 eV (Figure 2a and Supplementary Figure S6b). These contributions likely arise from platinum(II) and platinum(IV), [27] respectively, indicating that the sample is a mixture of the two oxidation states. [20, 21, 28] The (Pt/Ar) is well fitted by a single peak centred at 73.0 ± 0.1 eV arising from the +2 oxidation state. [29, 30] These oxidation-state assignments are consistent with the XANES spectra shown in Figure 2b. Here, reference spectra for PtCl_2 (+2) and $(\text{NH}_4)_2\text{PtCl}_6$ (+4) have white line peak positions at 11565.8 eV and 11567.7 eV, respectively. The spectrum for (Pt/Ani/Ar) has a single peak centred at 11566.7 eV. This is expected of a mixture of platinum(II) and platinum(IV) and is consistent with the XPS data.

[28, 29]

EXAFS spectra plotted in Figure 2c (along with those of the standards) give information about the platinum bonding environment. The standard samples of PtCl_2 and $(\text{NH}_4)_2\text{PtCl}_6$ have one dominant peak in the range of 1.5 to 2.3 Å with the centre at 1.96 Å, suggesting that this peak can be associated with Pt-Cl bonding. The most intense peak in the spectrum for (Pt/Ani/Ar) is at 1.96 Å with a shoulder at 1.66 Å. The peak at 1.96 Å should arise from the presence of Pt-Cl bonds. This shoulder peak at 1.66 Å is indicative of platinum-nitrogen bonding. [31, 32] Finally, there is absence of obvious Pt-Pt bonding at 2.73 Å (green curve in Figure 2c), which also suggests that the platinum atoms are mainly isolated from each other. We therefore

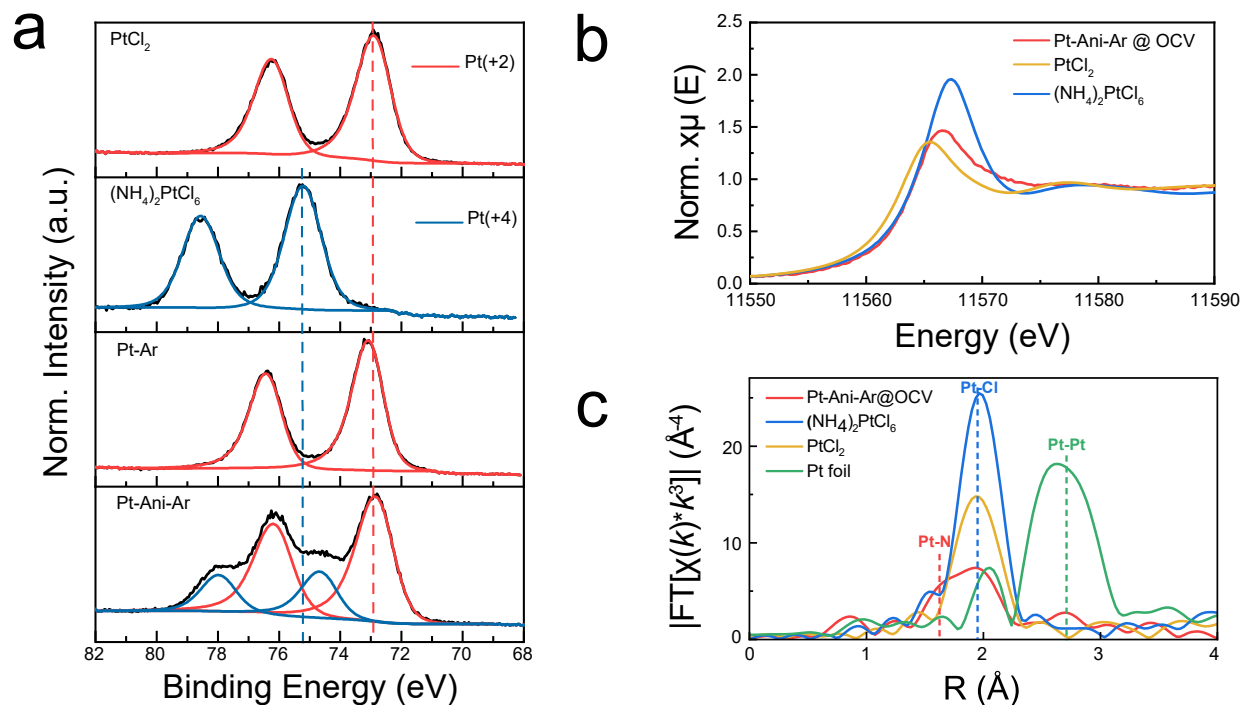


Figure 2. a,b, XPS spectra of Pt 4f (a) and XANES spectra (b) recorded at Pt L₃-edge for the synthesised Pt SSC and control sample (Pt/Ar) compared with reference standards in the oxidation states of platinum(II) and platinum(IV). The vertical dashed red and blue lines in (a) indicate the peak positions of Pt_{7/2} at the oxidation state of platinum(II) and platinum(IV). c, Corresponding k³-weighted Fourier-transformed Pt L₃-edge EXAFS spectra of samples in (b) and standard Pt foil. The vertical dashed lines show the positions of Pt-N (red), Pt-Cl (blue), and Pt-Pt (green) peaks.

interpret these data to mean that the aniline and chloride coordinate to the platinum to form a complex molecule.

These XPS and XANES data indicate that (Pt/Ani/Ar) and (Pt/Ar) are reduced in situ from platinum(IV) (the oxidation state of platinum in the precursor H₂PtCl₆) to platinum(II). This is likely caused by the ethanol solvent (Supplementary Figure S5). [33] However, in (Pt/Ani/Ar) the platinum forms a complex with the aniline (as confirmed by the bonding data from the EXAFS spectra) which decreases the platinum reduction potential. This is the reason that (Pt/Ani/Ar) is only partially reduced, with platinum(IV) still present. The STEM, XPS, XANES and EXAFS data, suggest that the aniline-treated sample contains atomically dispersed platinum in the form of molecular complexes (Pt single-site complexes) physisorbed onto the graphene substrate.

Operando XAS measurements

Operando hard XAS at the platinum L₃-edge was performed at different potentials to investigate the evolution of the platinum single-site complex's oxidation state and chemical bonding environment during HER. [18, 34, 35] A customised three-electrode cell setup (Supplementary Figure S8) was mounted to investigate the aniline-treated sample (Pt/Ani/Ar). The chronoamperometric performances of (Pt/Ani/Ar) at various potentials are shown in Figure 3a (with a particular shown in Figure 3a) at least 1000 s of operation at each of 10 voltages: 0.4, 0.3, 0.2, 0.1, 0.06, 0.02, 0, -0.02, -0.04, and -0.06 V versus the reversible hydrogen electrode (RHE). The open-circuit voltage (OCV) is 0.6 V versus RHE. None of the tests at a positive potential has an areal current density greater than 0.1 mA cm⁻². This is to be expected since the HER is only thermodynamically favourable below 0 V

versus RHE. Indeed, the data for the test at 0 V show a minimal areal current density until about 600 s (out of approximately 1200 s in total) when the current jumps suddenly and then gradually increases to about -0.3 mA cm^{-2} . The areal current densities for the subsequent potentials of -0.02, -0.04, and -0.06 V versus RHE are -0.5, -0.9, and -1.5 mA cm^{-2} , respectively. The Tafel slope, calculated using the 4 negative potentials, is 60 mV dec^{-1} . This is comparable to the Tafel slope of platinum nanoparticles for the HER. [36, 37]

The average of 8 XANES spectra, collected during operation at each potential, are shown in Figure 3c. These data show that the oxidation state of platinum decreases from a mixture of +4 and +2 to 0. When the potential is decreased from 0.6 V (OCV) to 0 V versus RHE, the positions of both the white line (red arrow and right inset in Figure 3c) and absorption edge (left inset in Figure 3c) in the XANES spectra show a negative shift of 0.4 eV. Those shifts suggest a continuous decrease of platinum valence from a mixture of platinum(II) and platinum(IV) to metallic platinum. [19, 38]

The bonding environment of the platinum also changes as the applied potential varies, as shown in the EXAFS spectra in Figure 3d. As the potential is decreased from OCV to 0, the peaks at 1.66 and 1.96 Å, arising from Pt-N and Pt-Cl bonds, respectively, both decrease in intensity. But the peak arising from Pt-N (blue vertical line) decreases faster than that arising from Pt-Cl (orange vertical line). This indicates that as the potential is decreased from OCV and while the oxidation state of the platinum falls to 0, the aniline molecules are dissociating from the complex. The chloride ions are also dissociating from the platinum atoms, but to a lesser extent compared to the aniline molecules. At 0 V, the SSC has two distinct EXAFS spectra (yellow and olive curves in Figure 3d and isolated in Figure S10): one at the low areal current density (-0.1 mA cm^{-2}) before the onset of the HER and one at the higher areal current density (-0.3 mA cm^{-2}) after the onset of the HER. Before the onset of the HER, the bonding environment still shows appreciable Pt-Cl bonding and some Pt-N bonding. After 600 s and the beginning of hydrogen evolution, almost all Pt-N bonding character is lost and the Pt-Cl bonding feature decreases significantly. The EXAFS spectrum is instead dominated by Pt-Pt bonding. The rapid breaking of Pt-N and Pt-Cl bonds at 0 V may be caused by hydrogen molecules aggregated on the SSC.

It has been experimentally shown that the diffusion and agglomeration of platinum atoms can be induced by exposure to a hydrogen atmosphere. [39–41] Since more reduced platinum structures after 600 s can boost the evolution of hydrogen by lowering the Gibbs free energy of hydrogen adsorption in acidic electrolytes, [19, 42] the sudden increase in current density here (discussed in Figure 3a) can probably be justified accordingly.

Structure-electrochemistry correlation

The previous section elucidates the evolution of the Pt single-site complex into metallic nanoclusters at potentials below 0 V; the details of this transformation need to be quantitatively examined together with catalytic activity. The effect of applied potential on both areal current density and platinum oxidation state in the SSC is shown in Figure 4a. The height of the XANES normalised white lines is summarised (black plot in Figure 4a) to quantify the evolution of platinum’s oxidation state and the electron occupancy of platinum’s $5d$ orbitals. [43, 44] The white-line height decreases precipitously from OCV (0.60 V) to about 0 V versus RHE. This is consistent with the complete filling of the platinum $5d$ valence orbitals and the formation of metallic platinum. [19] At the same potential, the corresponding areal current density increases precipitously as the HER becomes thermodynamically favourable, although they are still relatively low (from -0.001 to -0.08 mA cm^{-2}). There is an obvious drop in white-line height at around 0 V, and the white-line height stabilises at around 1.30 after 0 V, indicating the oxidation state of platinum remains as 0 at potentials below 0 V. Corresponding to the decrease in oxidation state, a significant increase in current density is also recorded at 0 V (red plot in Figure 4a). And after the increase, a linear relationship between the base-10 logarithm of the areal current density and the potentials is presented.

EXAFS curve-fitting analysis on the platinum’s EXAFS spectrum at OCV allows for the determination of a plausible molecular structure for the platinum complex adsorbed onto graphene. Considering 8 possible platinum complex molecules described by $(\text{C}_6\text{H}_5\text{NH}_2)_x\text{Cl}_y\text{Pt}$ for $x = 1$ or 2 and $y = 1, 2, 3,$ or 4 , the Pt-N and Pt-Cl bond lengths (about 2.05 Å and 2.30 Å, respectively) determined by density-functional theory modelling of the isolated molecular complexes are the

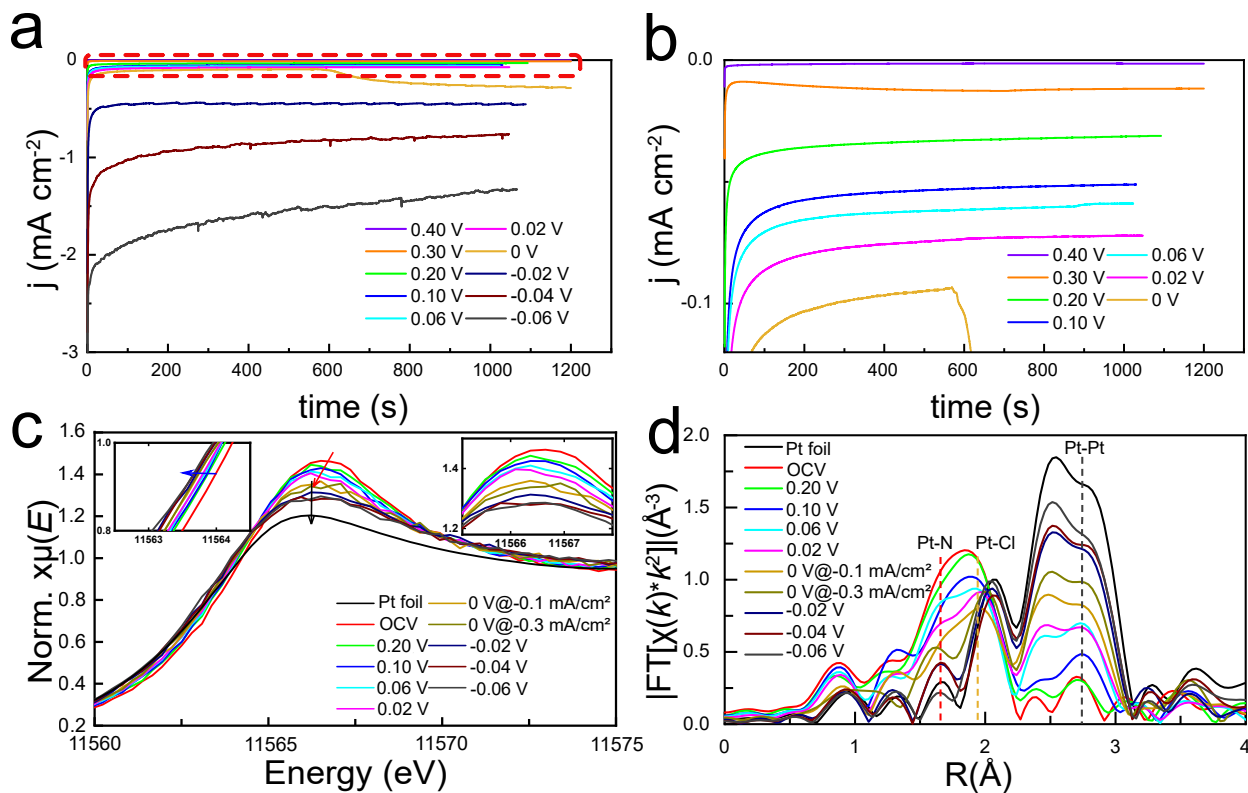


Figure 3. **a**, Stable chronoamperometric curves of Pt single-site complex at variable applied potentials; **b**, Enlarged red dashed area in **(a)** shows the chronoamperometric curves at current density smaller than 0.1 mA cm^{-2} ; **c**, Operando XANES spectra recorded at Pt L_3 -edge of synthesised Pt single-site complex sample at different working potentials for HER in $0.5 \text{ M H}_2\text{SO}_4$. The inset graphs show the energy shifts of Pt L_3 absorption edge (left) and white-line peak (right). **d**, The corresponding K^2 -weighted Fourier-transformed EXAFS spectra (magnitude component). The vertical dashed lines show the Pt-N (red), Pt-Cl (orange) and Pt-Pt (grey) peaks.

starting point for the analysis. The operando EXAFS data are best described by the structural model for *trans*-dianilinedichloroplatinum(II), $(\text{C}_6\text{H}_5\text{NH}_2)_2\text{Cl}_2\text{Pt}(\text{II})$, within the fitting range (K range: 3 to 12.5 \AA^{-1} , R range: 1.1 to 2.5 \AA^{-1} , misfit factor 0.8%). This structure is similar to the previously reported crystal $(\text{C}_6\text{H}_5\text{NH}_2)_2\text{PtCl}_2$ complex, prepared by mixing aniline with H_2PtCl_6 . [45, 46]

Performing EXAFS curve-fitting analysis (platinum's first (1.5 to 2.1 \AA) and second (2.3 to 3.1 \AA) coordination shells) on the spectra collected at different potentials results in the curves in Figure 4b and Table S1, which shows the average number of platinum, chlorine, and nitrogen atoms coordinated to each platinum atom (i.e. the coordination number), as a function of applied

potential. Specifically, Figure 4c highlights the evolution of the EXAFS spectra while decreasing potential in the R-space fitted with the contributions of Pt-N, Pt-Cl and Pt-Pt paths. At OCV, the coordination number for both chlorine and nitrogen is about 2.5 . As the potential is lowered, the coordination number for nitrogen decreases to about 1.0 by a potential of 0.1 V versus RHE. It continues to decrease to about 0.5 by 0 V (but before the onset of the HER). The chlorine coordination number stays higher than the nitrogen coordination number. This indicates that the aniline molecules dissociate from the complex before the chloride ions do, likely due to the more ionic character and higher bond energy of the Pt-Cl bonds compared to the Pt-N bonds. [47] The platinum coordination number increases as the potential is lowered, ultimately reaching a value

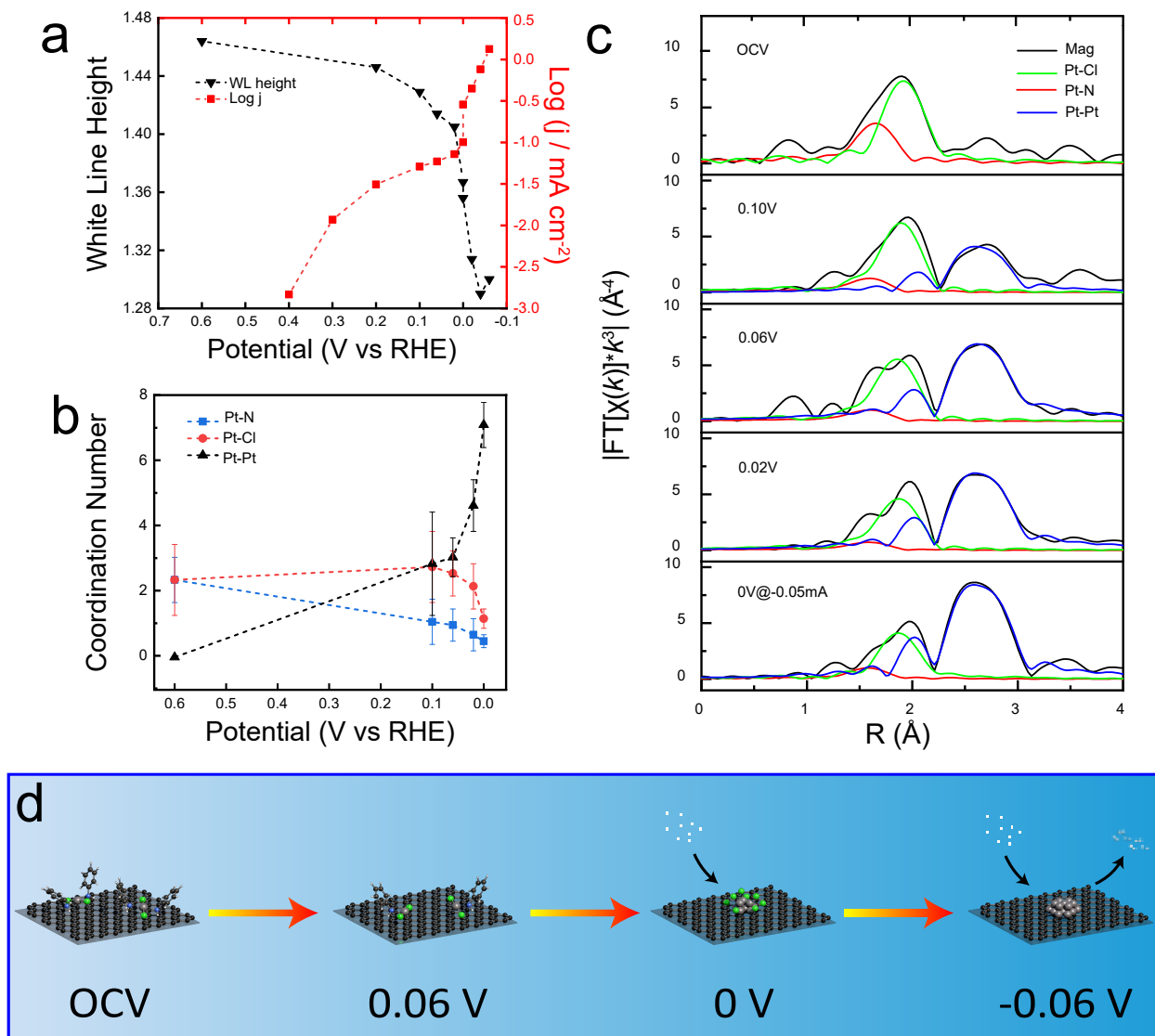


Figure 4. **a**, Amplitude of normalised white-line peak of Pt L_3 -edge operando XANES spectra (black) and the corresponding catalytic activity (red) at different potentials. Log(j) is calculated using relatively stable current density at the end of each CA test. **b**, Coordination number of Pt-N, Pt-Cl and Pt-Pt fitting paths for operando EXAFS data of Pt single-site complex at selected potentials by 0 V. Error bars in **(b)** represent the uncertainties of fitting results. **c**, Contribution of different paths (Pt-N, Pt-Cl and Pt-Pt) to fit the corresponding EXAFS spectra. The details of the fitting results shown in K-space and R-space can be found in Supplementary Figure S11. **d**, Proposed schematic model for the evolution of (Pt/Ani/Ar) sample from single-site complex to subnanocluster based on the operando EXAFS analysis (grey, Pt; green, Cl; blue, N; black, carbon; white, H).

of about 7.0 by 0 V versus RHE. This indicates the agglomeration of platinum as the potential is lowered, which is also in line with the reduction of the oxidation state of platinum described in Figure 4a. [48]

Together these data elucidate how the platinum bonding environment in an SSC changes as a function of applied potential during operation, as described schematically in Figure 4d. As the potential is lowered from OCV, the dianilinedichloroplatinum(II) decomposes as the aniline dissociates from the platinum first, followed by the dissociation of the chloride ions. Simultaneously, the 5*d* valence orbitals of platinum are filled. By the onset of the HER at 0 V versus RHE, the dianilinedichloroplatinum(II) complexes have completely dissociated, and the metallic platinum(0) single atoms agglomerate into nanoclusters which catalyse the HER.

Conclusions

In this work, we use operando, synchrotron X-ray absorption spectroscopy to characterize how the oxidation state and bonding environment of platinum changes in an SSC for the HER at the molecular level. First we show successful synthesis of a platinum SSC, confirming the platinum is atomically dispersed by STEM and XRD. We observe a mixture of platinum(II) and platinum(IV) by XPS and XANES, and we confirm platinum coordination to aniline by ex situ EXAFS. We then probe the oxidation state and molecular structure as a function of applied potential using operando EXAFS and XANES with synchrotron radiation. We find that as the potential is lowered from OCV the platinum oxidation state decreases, breaking bonds between platinum atoms and aniline ligands first. The Pt-Cl bonds also break, but to a lesser extent than the Pt-N bonds. Finally, once the onset of the HER at 0 V versus RHE is reached, the platinum is completely reduced and metallic platinum atoms agglomerate to form catalytic nanoclusters. Our work suggests that many catalysts that achieve atomically dispersed platinum by aniline coordination do not remain atomically dispersed during device operation. This complicates the interpretation of many experimental results. Furthermore, this operando study establishes two important structure-property relationships for aniline-complex platinum SSCs. First, platinum exists as metallic platinum (that is, in the oxidation state 0) while catalysing the HER. Second, the

molecular structure of the platinum complexes is lost by the onset of the HER. These findings are an important contribution to atomic understanding of structural evolution of SSCs for the HER and the development of high-performance platinum SSCs for clean hydrogen production.

Declaration of interest

The authors declare no competing interests.

Data availability

The authors declare that all data supporting the findings of this study are included within the paper and its Supplementary Information files. Source data are available from the corresponding author upon reasonable request.

Acknowledgements

The authors would like to acknowledge the financial support of the Jiangsu Industrial Technology Research Institute (JITRI) and the Henry Royce Institute (through UK Engineering and Physical Science Research Council grant EP/R010145/1) for capital equipment. We acknowledge Diamond Light Source for time on B18 Beamline under Proposal SP-26066. We are grateful to the David Cockayne Centre for Electron Microscopy for the use of their electron microscopes.

Author contributions

P.T and M.P conceived and designed the experiments. P.T prepared the samples and performed the electrochemical tests. P.T, J.C and J.H.W performed the aberration-corrected STEM characterisation and analysed the data. D.G and R.A conducted the operando XAFS experiments at Diamond Light Source under the proposal of SP.26066. P.T and H.J.L analysed the operando XAFS data. P-Y.H and P.T prepared reference samples and calibrated the three-electrode cell used in operando XAFS study. S.N performed the XPS characterisation and contributed to XPS data interpretation. K.H conducted the DFT calculations. P.T, K.H and C.W wrote the manuscript with input

from all authors. M.P. supervised the design of the project and gave frequent, in-depth scientific input.

Experimental procedures

Chemicals

Chloroplatinic acid hexahydrate (37.5% Pt basis), aniline (99.5%) and ammonium persulfate (98%) were purchased from Sigma-Aldrich. Ultra-pure water (18.2 M Ω cm⁻¹; by Direct-Q Water Purification System) was used for the electrochemical tests.

Synthesis of Pt single-atom/clusters at surface of graphene

The Pt single-site complex catalysts stabilised on the surface of thin-layer graphene by aniline molecules was prepared using a modified impregnation method. [10] Firstly, thin-layer graphene is grown by a CVD method, and transferred onto the surface of well-polished glassy carbon (GC). [49] Then, graphene surface is cleaned by annealing under Ar (70 sccm) / H₂ (5 sccm) flow at 250 °C for 2 hours. The remaining sulphur from ammonium persulfate and small organics are removed. Then samples with different Pt structures are synthesised on the clean surface of graphene. Sample one (**Pt/Ani/Ar**): 4 μ L of aniline drop casted on a 1 cm² graphene nanosheets, dried in ambient conditions for 15 minutes, then drop casting 10 μ L of 10 mM/L H₂PtCl₆ ethanol solution. It is then annealed in argon atmosphere at 100 °C for 1.5 h. Sample two (**Pt/Ar**): synthesised using the same procedure without drop casting aniline. For further comparison, samples are prepared by annealing (Pt/Ani/Ar) at 200 °C instead of 100 °C (**Pt/Ani/Ar/200 °C**), and replacing argon annealing condition with hydrogen annealing condition (**Pt/Ani/H₂**). After the annealing treatment, all samples are sequentially washed with 0.5 M sulfuric acid then deionized water, and dried under vacuum overnight.

Ex-situ STEM and XRD

Room-temperature annular dark-field scanning transmission electron microscopy was performed with a JEOL ARM200F at an accelerating voltage of 80 kV. Dwell times of 10-20 μ s, a beam current of 35 pA, and a pixel size of 0.006 nm px⁻¹ were used for imaging, with a convergence semi-angle

of 25.5 mrad and collecting inner-outer angles 68 to 275 mrad. XRD patterns were collected using a monochromated Cu K α X-ray source from 5° to 90° (2 θ), at a scan rate of 5°min⁻¹.

Ex-situ XPS and XAS

X-ray photoemission spectroscopy was conducted using a PHI VersaProbe III system generating monochromatic Al X-rays at 1486 eV. Survey scans and high-resolution elemental scans were acquired at pass energies of 224 eV and 55 eV respectively. The binding energies were calibrated using the C 1s line at 284.8 eV as reference. The XPS spectra were fit using Gaussian-Lorentzian and Voigt lineshapes (where asymmetry was pronounced), and quantified with the help of CasaXPS software. X-ray absorption fine structure (XAFS) measurements at the Pt L₃ edge were carried out at the B18 Core EXAFS beamline of Diamond Light Source. The Pt reference samples (300 mg) were finely ground, mixed homogeneously with five parts of cellulose and pressed into 13 mm diameter pellets. Commercial (NH₄)₂PtCl₆ (Sigma-Aldrich, 99.9%), PtCl₂ (Sigma-Aldrich, 99.9%) were used as references. All spectra were recorded in transmission mode at room temperature.

Electrochemical measurements

The catalytic activity of synthesised samples were evaluated under a three-electrode cell with graphite rod as counter electrode and Ag/AgCl (in 3M KCl) as reference electrode in 0.5M Ar/N₂-purged H₂SO₄ solution. A 0.2 mm thick well-polished glassy carbon plate (Sigma-Aldrich Company Ltd.) was firstly used to transfer and support the thin-layer graphene nanosheets. Then the GC supporting well-dispersed Pt catalysts with (1 cm \times 1 cm) defined area was used as the working electrode. A metal clip was used to connect the working electrode with an external circuit. The chronoamperometric performances were recorded by a Ivium Technologies or Biologic VMP3 potentiostat. All potentials were calibrated versus RHE using $E(\text{RHE}) = E(\text{Ag/AgCl}) + 0.197 \text{ V} + 0.0592 \times \text{pH}$.

Operando XAS

EXAFS and XANES were performed at the B18 Core EXAFS beamline of Diamond Light Source. The measurements were carried out using the Cr-coated

branch of collimating and focusing mirrors, and a Si(111) double-crystal monochromator. The size of the beam at the sample position was ca. 1mm (h)×1mm (v). Samples were measured both in static electrolyte and operando conditions. The data were collected in fluorescence mode, by means of a 36-element solid state germanium detector, the ion chamber at the front of the sample has been used for measurement of incoming photons (I_0 filled with a mixture of 80 mbar of Ar and 1020 mbar of He to optimise sensitivity at 15% efficiency). An electrochemical cell adapted to the B18 beamline of the UK’s Synchrotron Diamond Light Source was designed for the operando study shown in Supplementary Figure S8. Before the operando electrochemical measurements, the Pt L_3 edge spectra were measured on contact with the liquid electrolyte. The operando XAFS spectra of the Pt L_3 edge (11564 eV) were obtained from 200 eV before the edge up to 750 eV after the edge (corresponding to 14 \AA^{-1} in k-space). The measuring time was 2 minutes per spectrum. When indicated, 8 repetitions at each potential were acquired and then merged to obtain a better signal to noise ratio. Data were normalised using the Athena [50] program with a linear pre-edge and polynomial post-edge background subtracted from the raw data. EXAFS fits were performed using ARTEMIS software. [50]

Computational methods

DFT calculations were performed using the Vienna ab initio Simulation Package (VASP) [51, 52]. We performed Γ -point only calculations using a plane-wave kinetic-energy cutoff of 520 eV with electronic and ionic convergence criteria of 10^{-5} eV and 0.05 eV \AA^{-1} , respectively. The Perdew-Burke-Ernzerhof (PBE) functional was used for all structures.

References

1. *Hydrogen From Renewable Power: Technology outlook for the energy transition* (IRENA, 2018).
2. Lagadec, M. F. & Grimaud, A. Water electrolyzers with closed and open electrochemical systems. *Nature Materials* **19**, 1140–1150 (2020).
3. McCrory, C. C. *et al.* Benchmarking hydrogen evolving reaction and oxygen evolving reaction electrocatalysts for solar water splitting devices. *Journal of the American Chemical Society* **137**, 4347–4357 (2015).
4. Cui, X., Li, W., Ryabchuk, P., Junge, K. & Beller, M. Bridging homogeneous and heterogeneous catalysis by heterogeneous single-metal-site catalysts. *Nature Catalysis* **1**, 385–397 (2018).
5. Kibsgaard, J. & Chorkendorff, I. Considerations for the scaling-up of water splitting catalysts. *Nature Energy* **4**, 430–433 (2019).
6. Qiao, B. *et al.* Single-atom catalysis of CO oxidation using Pt_1/FeO_x . *Nature chemistry* **3**, 634–641 (2011).
7. Cheng, N., Zhang, L., Doyle-Davis, K. & Sun, X. Single-atom catalysts: from design to application. *Electrochemical Energy Reviews* **2**, 539–573 (2019).
8. Yang, X.-F. *et al.* Single-atom catalysts: a new frontier in heterogeneous catalysis. *Accounts of chemical research* **46**, 1740–1748 (2013).
9. Wang, A., Li, J. & Zhang, T. Heterogeneous single-atom catalysis. *Nature Reviews Chemistry* **2**, 65–81 (2018).
10. Ye, S. *et al.* Highly stable single Pt atomic sites anchored on aniline-stacked graphene for hydrogen evolution reaction. *Energy & Environmental Science* **12**, 1000–1007 (2019).
11. Xu, H., Cheng, D., Cao, D. & Zeng, X. C. A universal principle for a rational design of single-atom electrocatalysts. *Nature Catalysis* **1**, 339–348 (2018).
12. Chen, Y. *et al.* Single-atom catalysts: synthetic strategies and electrochemical applications. *Joule* **2**, 1242–1264 (2018).
13. Thomas, J. M., Raja, R. & Lewis, D. W. Single-site heterogeneous catalysts. *Angewandte Chemie International Edition* **44**, 6456–6482 (2005).
14. Pelletier, J. D. & Basset, J.-M. Catalysis by design: well-defined single-site heterogeneous catalysts. *Accounts of chemical research* **49**, 664–677 (2016).

15. Zhao, D. *et al.* Atomic site electrocatalysts for water splitting, oxygen reduction and selective oxidation. *Chemical Society Reviews* **49**, 2215–2264 (2020).
16. Wang, J., Dou, S. & Wang, X. Structural tuning of heterogeneous molecular catalysts for electrochemical energy conversion. *Science Advances* **7**, eabf3989 (2021).
17. Li, X., Yang, X., Zhang, J., Huang, Y. & Liu, B. In Situ/Operando techniques for characterization of single-atom catalysts. *ACS Catalysis* **9**, 2521–2531 (2019).
18. Maurer, F. *et al.* Tracking the formation, fate and consequence for catalytic activity of Pt single sites on CeO₂. *Nature Catalysis* **3**, 824–833 (2020).
19. Fang, S. *et al.* Uncovering near-free platinum single-atom dynamics during electrochemical hydrogen evolution reaction. *Nature communications* **11**, 1029 (2020).
20. Kaiser, S. K. *et al.* Nanostructuring unlocks high performance of platinum single-atom catalysts for stable vinyl chloride production. *Nature Catalysis* **3**, 376–385 (2020).
21. Ren, Y. *et al.* Unraveling the coordination structure-performance relationship in Pt₁/Fe₂O₃ single-atom catalyst. *Nature communications* **10**, 4500 (2019).
22. Fei, H. *et al.* Single atom electrocatalysts supported on graphene or graphene-like carbons. *Chemical Society Reviews* **48**, 5207–5241 (2019).
23. Lee, J. K. *et al.* Metal atom markers for imaging epitaxial molecular self-assembly on graphene by scanning transmission electron microscopy. *ACS Nano* **13**, 7252–7260 (2019).
24. Li, Y. *et al.* An oxygen reduction electrocatalyst based on carbon nanotube-graphene complexes. *Nature Nanotechnology* **7**, 394–400 (2012).
25. Li, X. *et al.* Precursor design for high density single Pt atom sites on MoS₂: enhanced stability at elevated temperatures and reduced 3D clustering. *Chemistry of Materials* **32**, 2541–2551 (2020).
26. Shiell, T. B. *et al.* In situ analysis of the structural transformation of glassy carbon under compression at room temperature. *Physical Review B* **99**, 024114 (2019).
27. Yang, M. *et al.* A common single-site Pt(II)-O(OH)_x- species stabilized by sodium on "active" and "inert" supports catalyzes the water-gas shift reaction. *Journal of the American Chemical Society* **137**, 3470–3473 (2015).
28. Liu, J. *et al.* High performance platinum single atom electrocatalyst for oxygen reduction reaction. *Nature communications* **8**, 15938 (2017).
29. Cheng, X. *et al.* Highly active, stable oxidized platinum clusters as electrocatalysts for the hydrogen evolution reaction. *Energy and Environmental Science* **10**, 2450–2458 (2017).
30. Imaoka, T. *et al.* Platinum clusters with precise numbers of atoms for preparative-scale catalysis. *Nature Communications* **8**, 688 (2017).
31. Lim, T. *et al.* Atomically dispersed Pt–N₄ sites as efficient and selective electrocatalysts for the chlorine evolution reaction. *Nature Communications* **11**, 412 (2020).
32. Li, X. *et al.* Single-atom Pt as co-catalyst for enhanced photocatalytic H₂ evolution. *Advanced Materials* **28**, 2427–2431 (2016).
33. Obreja, L., Foca, N., Popa, M. & Melnig, V. Alcoholic reduction platinum nanoparticles synthesis by chemical method, biomaterials in biophysics. *Medical Physics and Ecology* (2008).
34. Wang, J. *et al.* In Situ identifying the dynamic structure behind activity of atomically dispersed Platinum catalyst toward hydrogen evolution reaction. *Small* **17**, 2005713 (2021).
35. Cao, L. *et al.* Identification of single-atom active sites in carbon-based cobalt catalysts during electrocatalytic hydrogen evolution. *Nature Catalysis* **2**, 134–141 (2019).
36. Ghanim, A. H. *et al.* Low-loading of Pt nanoparticles on 3D carbon foam support for highly active and stable hydrogen production. *Frontiers in chemistry* **6**, 523 (2018).
37. Kang, J. *et al.* Platinum Atoms and Nanoparticles Embedded Porous Carbons for Hydrogen Evolution Reaction. *Materials* **13**, 1513 (2020).

38. Mansour, A., Cook Jr, J. & Sayers, D. Quantitative technique for the determination of the number of unoccupied d-electron states in a platinum catalyst using the $L_{2,3}$ X-ray absorption edge spectra. *The Journal of Physical Chemistry* **88**, 2330–2334 (1984).
39. Horch, S. *et al.* Enhancement of surface self-diffusion of platinum atoms by adsorbed hydrogen. *Nature* **398**, 134–136 (1999).
40. Parkinson, G. S. *et al.* Carbon monoxide-induced adatom sintering in a Pd-Fe₃O₄ model catalyst. *Nature Materials* **12**, 724–728 (2013).
41. Dessal, C. *et al.* Atmosphere-dependent stability and mobility of catalytic Pt single atoms and clusters on γ -Al₂O₃. *Nanoscale* **11**, 6897–6904 (2019).
42. Shi, Y. *et al.* Electronic metal–support interaction modulates single-atom platinum catalysis for hydrogen evolution reaction. *Nature communications* **12**, 3021 (2021).
43. Wang, J. *et al.* Redirecting dynamic surface restructuring of a layered transition metal oxide catalyst for superior water oxidation. *Nature Catalysis* **4**, 212–222 (2021).
44. Malta, G. *et al.* Identification of single-site gold catalysis in acetylene hydrochlorination. *Science* **355**, 1399–1403 (2017).
45. Mohanraju, K., Lee, H. & Kwon, O. J. High loading Pt core/carbon shell derived from platinum-aniline complex for direct methanol fuel cell application. *Electroanalysis* **30**, 1596–1601 (2018).
46. Kong, P. C. & Rochon, F. D. *Cis- and trans-platinum complexes of anilines. A study of isomerization reactions* 1982.
47. Astakhov, A., Soliev, S. & Chernyshev, V. Metal-ligand bond dissociation energies in the Ni, Pd, and Pt complexes with N-heterocyclic carbenes: effect of the oxidation state of the metal (0,+ 2). *Russian Chemical Bulletin* **69**, 2073–2081 (2020).
48. Hao, X. *et al.* Direct measurement and modulation of single-molecule coordinative bonding forces in a transition metal complex. *Nature communications* **4**, 2121 (2013).
49. Fan, Y., He, K., Tan, H., Speller, S. & Warner, J. H. Crack-free growth and transfer of continuous monolayer graphene grown on melted copper. *Chemistry of Materials* **26**, 4984–4991 (2014).
50. Ravel, B. & Newville, M. ATHENA, ARTEMIS, HEPHAESTUS: data analysis for X-ray absorption spectroscopy using IFEFFIT. *Journal of synchrotron radiation* **12**, 537–541 (2005).
51. Theory of the crystal structures of selenium and tellurium: The effect of generalized-gradient corrections to the local-density approximation. *Physical Review B* **50**, 13181–13185 (1994).
52. Kresse, G. & Furthmüller, J. Efficiency of ab-initio total energy calculations for metals and semiconductors using a plane-wave basis set. *Computational Materials Science* **6**, 15–50 (1996).